

Liquid-Crystalline Assembly of Sphere-Shaped Cellulose Nanocrystals

Li Cheng

Qingdao University of Science and Technology

Bingrui Liu

Qingdao University of Science and Technology

Jian Hu

Qingdao University of Science and Technology

Lijuan Zhou

Qingdao University of Science and Technology

Lu Zong

Qingdao University of Science and Technology

Yongxin Duan

Qingdao University of Science and Technology

Jianming Zhang

Qingdao University of Science and Technology

Yuan Yuan (✉ yuan yuan@qust.edu.cn)

Qingdao University of Science and Technology <https://orcid.org/0000-0002-5900-5303>

Research Article

Keywords: Sphere-like Cellulose Nanocrystals, Self-assembly, Liquid Crystals

Posted Date: March 10th, 2022

DOI: <https://doi.org/10.21203/rs.3.rs-1409924/v1>

License:   This work is licensed under a Creative Commons Attribution 4.0 International License.

[Read Full License](#)

Abstract

Rod-like cellulose nanocrystals (that is cellulose nanorods, CNRs) can self-organize into chiral nematic liquid crystals owing to their anisotropy character. Unexpected, sphere-like cellulose nanocrystals (cellulose nanospheres, CNSs) have been observed to form a chiral liquid crystalline phase also. Herein, to understand how the similar assembly take places as the particle dimension changes, the organization features of the CNSs were investigated. It reveals that CNSs organize into a liquid-crystal phase constituted by periodically parallel-aligned layer-structure above a critical concentration in suspension, the structure of which retains after drying. Compared with CNRs, the CNSs alignment shows short layer distance, low order degree, and weak long-range orientation. Considering the lower surface charge and the spherical appearance, a “knot-like” model which was captured by “freezing” the CNSs suspension in intermediate aggregation state, is proposed in the early stage of tactoid formation. Such structure acts as the fundamental unit to achieve the liquid-crystal assembly further.

Introduction

Cellulose is the most inexhaustible and renewable biomacromolecules in nature. It is characterized as a linear polymer formed by a $\beta(1, 4)$ -D-glycosidic bond connecting several glucose residues (the chemical structure is shown in Fig. 1). Natural cellulose is a kind of crystalline polymer. The nanocrystal with high crystallinity is obtained by removing the amorphous regions further. Cellulose nanocrystal (CNC) exhibits combined advantages in abundance, recyclability, large specific surface area, high stiffness, and the abilities of chemical modification and physical assembly (Klemm et al., 2011). It shows great potential in a wide range of applications consequently. One of the most promising one is the production of optical materials by controlling the underlying structure, which is correlation with the liquid-crystal organization of CNCs (Lagerwall et al., 2014; Parker et al., 2018; Prathapan et al., 2020; Tao and Xu, 2020).

CNCs are normally isolated from native cellulosic materials by acid hydrolysis, mostly by sulfuric acid (Mahmud et al., 2019; Xie et al., 2018). The hydrolysis reaction occurs from the cellulose surface to the inner amorphous region, leading to the typical rod-like shape of CNCs observed as early as 1953 (Hasegawa et al., 2020; Mukherjee and Woods, 1953; Ureña-Benavides et al., 2011; Wang et al., 2020). CNCs feature the ability to self-organize into a lyotropic liquid crystal, the understanding to which is almost targeted at rod-shaped nanocrystals. The acid hydrolysis produces CNCs with negatively charged groups on the surface. As diluted in water, an isotropic dispersion is obtained firstly (Revol et al., 1992). After achieving a balance between the rotational and translational entropies of individual nanorods with increased concentration as demonstrated by Onsager (Onsager, 1949), the rodlike crystallites start to align attributed from the anisotropic diffusion (Zero and Pecora, 1982). Thus formed microdomains grow into a short-range ordered structure called tactoid (Wang, et al., 2016) in which the CNCs show a chiral nematic order with the helical layer stacks (Revol et al., 1992). Specifically, CNC rods were aligned parallel to each other and to the plane of layers, each layer being rotated slightly with respect to the ones above or below it. Through the subsequent fusion and precipitation between tactoids, the long-range ordered chiral nematic liquid crystals (or called cholesteric liquid crystals) showing characterized birefringence are

organized. The hierarchical structure found in the suspension can be preserved further in the solid state upon complete evaporation of water (Parker et al., 2018).

Besides rod-shaped ones, a type of sphere-like CNCs that is the so-called cellulose nanospheres (CNSs) has been reported since 2001 (Cheng et al., 2014; Li, et al., 2001; Wang et al., 2008). CNSs were generally produced by appropriate pre-treatment in a combination of ultrasonic-assisted hydrolysis to cellulosic materials (Meyabadi et al., 2014; Yu et al., 2014; Zhang et al., 2007; Zianor Azrina et al., 2017). Interestingly enough, as the solid content was above a critical value, a liquid crystalline phase in the suspension of CNSs with high polydispersity was observed by Wang et.al. (Wang et al., 2008). To our best knowledge, the mechanism of the liquid crystalline formation in CNSs suspensions is limited to the deduction that the presence of the negatively charged groups on CNSs surface changes the effective particle shape (Wang et al., 2008). It is far from the complete understanding to the liquid-crystal behavior of cellulose nanocrystals as the particle dimensions changes from rod shape to the sphere one.

In this work, sphere-like cellulose nanocrystals (CNSs) as well as rod-like ones (CNRs) in different aspect ratio were prepared using a comparable preparation strategy of sulfuric acid hydrolysis. The self-assembly of the CNSs from suspension to the solid state was investigated in detail subsequently. Based on morphology observation combined with structure analysis, features of CNSs liquid-crystal formation was revealed by comparing with the CNRs. In order to Fig out the assembly mechanism further, the intermediate state in the CNSs organization was frozen in a polyacrylamide (PAAm) matrix by photopolymerization (Wang et al., 2016; Wang et al., 2020). CNSs aggregation structures locked in PAAm were captured by scanning electron microscopy (SEM). The assembly model is constructed consequently.

Experimental Section

Materials.

Cotton pulp with a cellulose polymerization degree (DP) of 900 was supplied by Silver Hawk Co. Ltd. (Gaomi, China). Sulphuric acid (H_2SO_4 , 95–98 wt.%), sodium hydroxide (NaOH), and dimethyl sulfoxide (DMSO) with analytical grade were purchased from Sinopharm Chemical Reagent Co. Ltd. (Shanghai, China). Dialysis bags (molecular weight cut-off or MWCO 8,000–14,000; 25 mm) were purchased from Sigma-Aldrich. Deionized water was used throughout all experiments.

Pretreatment of Cotton Pulp.

The cotton pulp was mixed with 4 wt.% NaOH solution and heated to 80°C for 3 h. The mixture was filtered and washed with deionized water to neutral pH. Then the treated pulp was dried at 60°C in an oven for 24 h. Such obtained cotton pulp named as pulp-a was used to prepare rod-shaped CNCs with large aspect ratio (LCNRs) and small aspect ratio (SCNRs). Next, the dried pulp was mixed with 150 ml of DMSO and heated to 80°C for 3 h in a water bath. The obtained pulp slurry was filtered and washed with deionized water to remove unwanted substances, and then dried at 60°C in an oven for 24 h. Such

obtained cotton pulp named as pulp-b was used to prepare sphere-shaped CNCs that is the cellulose nanospheres (CNSs).

Preparation of CNCs Suspensions and Films.

Preparation of LCNRs and SCNRs Suspensions.

The hydrolyzed of Pulp-a was carried out in 64 wt.% H_2SO_4 solution (9 mL for 1 g pulp) with vigorous stirring (500 rpm) at 45°C for 90 min. The reaction was stopped by diluting the suspension with 20 times amount of water. Then the remaining suspension was repeatedly centrifuged for 10 min at 8000 rpm in a refrigerated centrifuge to remove the supernatant. The dilution and centrifugation cycle were repeated until the CNCs remained in suspension after centrifugation. Last step, the suspension was transferred into the dialysis bag for further sample preparation.

The hydrolyzed of Pulp-a was carried out in a 64 wt.% H_2SO_4 solution (9 mL for 1 g pulp) in an ultrasound bath (the frequency was set as 40 kHz, the ultrasonic power was set as 320 W) with vigorous stirring (500 rpm) at 45°C for 2 h. The subsequent centrifugation procedure is the same as that described above.

Preparation of CNSs Suspension.

Pulp-b was firstly hydrolyzed in a 64 wt.% H_2SO_4 solution (9 mL for 1 g pulp) in an ultrasound bath at 45°C for 2 h. The mechanical stirring was performed at 500 rpm during hydrolysis. Then 2 or 3 times amount of deionized water was added to the suspension with continued ultrasonic treatment for further 30 minutes. The subsequent centrifugation procedure is the same as that described above.

Preparation of CNCs Films.

Three types of CNCs suspensions were firstly transferred into dialysis bags and concentrated in polyethylene glycol (DP = 20000) to a concentration of 6 wt.%. Then 2 mL of concentrated suspension was cast in an uncovered polystyrene petri dish with the diameter of 35 mm under ambient conditions. It took ca. 1.5 days for the film to be dried. The thickness of the as-prepared film is about 300 μm .

Characterizations

Transmission Electron Microscopy (TEM).

The shape and size of CNC samples were investigated on the transmission electron microscope (JOEL, JEM-2100, Japan) at 200 kV. The CNC suspensions were diluted by deionized water to about 0.1 wt.% concentration. One drop of suspension was transferred on a copper grid, dried for 1 min under an infrared lamp and then stained with phosphotungstic acid at a concentration of 3 wt.%. Particle size and the size distribution of the samples were determined from the analysis of TEM images by using the Nano Measurer software.

Scanning Electron Microscopy (SEM).

The morphology of CNC samples was investigated using the scanning electron microscope (JOEL, JSM-7500F, Japan) at an acceleration voltage of 5 kV. The samples were observed by dropping a dilute CNC suspension onto the carbon tape on aluminum stubs and then gold-coated by ion sputtering to make them conductive prior to the analysis.

Atomic Force Microscopy (AFM).

AFM (Bruker Dimension Icon AFM, USA) measurement was performed under Scanasyt air mode. The dimensions of the CNCs were determined from the analysis of their area in a 5 μm scan image by using the nanoscope software. Before testing, a dilute CNSs suspension (0.1 mg/mL) was spin-coated on freshly cleaved mica at 2000 rpm for 1 min.

Optical Measurements.

Cross-polarized images of samples in colorimetric plates were photographed by placing the colorimetric plate between two linear polarizers placed at 90° with a mobile phone. Polarized optical micrographs (POM) were obtained on a polarized optical microscope (Nikon, ECLIPSE LV100, Japan).

Dynamic Light Scattering (DLS).

Diffusion coefficient, hydrodynamic diameter, and zeta-potential of the as-prepared CNCs were determined on a Zeta sizer Nano ZS90 (Malvern Instruments, UK). The measurements for 5–60 mg/mL CNC suspensions were conducted in triplicate for each sample. CNC dispersions were prepared using deionized water as the dilution media.

Wide-angle X-ray Diffraction (WAXD).

WAXD measurement was performed on the X-Ray diffractometer (Rigaku, SmartLab, Japan) with Cu K α radiation ($\lambda = 0.154 \text{ nm}$) in the diffraction angle range of 5–40° at a scanning rate of 5° min⁻¹. The degree of crystallinity (CrI) was calculated using the empirical equation (Azubuike et al., 2011; Segal et al., 1959).

$$\text{CrI}(\%) = \left(\frac{I_{200} - I_{\text{am}}}{I_{200}} \right) \times 100 \quad (1)$$

where CrI expresses the relative degree of crystallinity, I_{200} is the maximum intensity of the (200) lattice diffraction, I_{am} is the intensity of amorphous diffraction located at $2\theta = 18^\circ$ for cellulose I modification. Prior to measurement, the suspension was freeze-dried into powder and pressed into flakes.

UV - Vis Spectroscopy.

The light transmittance (% T) of the solid CNC films was acquired on a UV-Vis spectrophotometer (Shimadzu, UV-2550, Japan). The spectra were collected over the 300 – 800 nm spectrum range.

Capturing the Intermediate State of the CNSs Arrangement.

0.4 g acrylamide (monomer), 40 mg N,N'-methylenebisacrylamide (cross-linker) and 20 mg 2,2-diethoxyacetophenone (photoinitiator) were mixed with 4 ml CNSs suspension (6 wt.%). The homogeneous mixture was allowed to stand in the dark for 12 h and 3 days. Then the 300-nm ultraviolet-B light source (8 W) was used in the photo-polymerization process. Ultraviolet irradiation was applied for 20 min to give CNC–PAAm composite hydrogels. Samples for SEM imaging were obtained by heating the hydrogels in air at 60°C for 12 h, followed by breaking the resulting hard and brittle plastic blocks into small pieces using a hammer.

Results And Discussion

Self-Assembly of Sphere-like Cellulose Nanocrystal (CNSs) from Suspension to the Solid State.

Up to now, several methods were reported to obtain CNSs successfully including acid hydrolysis (Lu and Hsieh, 2010; Mahmud et al., 2019; Wang et al., 2008; Yu et al., 2014; Zhang et al., 2007; Zianor Azrina et al., 2017), sono-chemical-assisted hydrolysis (Filson & Dawson-Andoh, 2009), enzymatic hydrolysis (Meyabadi et al., 2014), hydrolysis using anaerobic microbial consortium (Satyamurthy and Vigneshwaran, 2013) or using ammonium persulfate (Cheng et al., 2014), ionic liquid processing (Al Hakkak et al., 2019; Babicka et al., 2020; Han et al., 2013; Sui et al., 2008), etc. In this work, the CNSs preparation was based on a method of NaOH and DMSO pretreatment in a combination of ultrasonic-assisted H₂SO₄ hydrolysis (Azrina et al., 2017) (the schematic route is shown in Fig. 1). Hydrolysis using sulfuric acid produces cellulose nanocrystals with sulfate ester groups on the surface (Mahmud et al., 2019; Xie et al., 2018), which is proved by the FTIR spectrum as shown in **Fig S1** in the supporting information.

The morphology of the CNSs as prepared was characterized firstly. The regular sphere-like particles in nanoscale (or called nanospheres) are observed clearly in SEM image as shown in Fig. 2**(a)**. Particle size was evaluated furthermore from TEM image. Based on statistical analysis of 138 individual nanospheres as shown in Fig. 2**(b)**, the diameter distribution of CNSs was extracted where all diameter coordinates (points) along the analyzed CNSs was plotted. As shown in Fig. 2**(c)**, the diameters of the CNSs are distributed in the range of 20–180 nm, 75% of which are in the range of 40–100 nm. The average diameter locates at ca. 78 nm. Moreover, our sphere-like cellulose nanocrystals take typical form I modification (Liu et al., 2020). The characteristic diffraction peaks respectively locate around 14.7, 16.5, 22.6, and 34.5° as shown in Fig. 2**(d)**, assigned to the corresponding (1–10), (110), (200), and (004) reflection planes. The crystallinity of the CNSs is calculated to be 91% according to the Eq. 1, which is higher than that of the reported ones in the 80–85% range generally (Ahmed-Haras et al., 2020; Wang et al., 2007; Yu et al., 2014; Azrina et al., 2017).

CNSs exhibit concentration-dependent phase behavior as dispersed in water. Figure 3**(a)** shows the aqueous suspension viewed in cuvette between cross-polarizers after two weeks of settling. The phase

behavior is distinguished into three regions, in which two critical concentrations of 2 and 5 wt.% are identified. The transparent suspensions in the low concentration of 0.5 and 1 wt.% are observed under polarized light. As the concentration increases from 2 to 4 wt.%, the suspension turns turbid. All of the suspensions in the 0.5-4 wt.% concentration range exhibit the flow birefringence under gentle shaking (as shown in **Fig S2** in the supporting information). Such birefringence pattern disappears within several seconds at rest. A biphasic pattern is observed for the CNSs suspension under 5 wt.% concentration. Part region of the suspension exhibits the remarkable birefringence, while the others still keep transparent as shown at the bottom. As the suspension is concentrated to 6 wt.% further, the cuvette is full of the bright birefringent texture.

To the rod-shaped cellulose nanocrystals (CNRs), the suspension shows a liquid crystalline texture above a critical concentration, which have been extensively studied (Ureña-Benavides et al., 2011; Zhou et al., 2018). As demonstrated by Onsager (Onsager, 1949), the translational entropy of individual CNRs contributes to such alignment mainly. Herein, the concentration-dependent phase behavior of the CNSs occurred in suspension is correlated with the liquid crystalline self-assembly also. In order to reveal the organization mechanism, the translation diffusion coefficient and the corresponding hydrodynamic diameter (D_h) as a function of concentration were measured by DLS firstly. Figure 3**(b)** shows that D_h of the CNSs keeps constant below 1 wt.% concentration, indicating the isolated dispersion of the particles. The diffusion coefficient decreases while the D_h increases as the concentration rises until 5 wt.%, reflecting the mobility of the CNSs turns weak due to the cooperativity in diffusion (Jiang et al., 2018). It indicates the onset of interparticle interaction above 1 wt.% concentration. The result from the DLS measurement is in agreement with that from the optical observation, showing the transition from isotropic phase to anisotropic liquid-crystal phase with increased concentration.

The evolution of the internal structure during CNSs phase transition was monitored on the suspension under characterized 5 wt.% concentration. Figure 4 and **Fig S3** in the supporting information record the time-resolved POM images of the suspension. As shown in Fig. 4**(a)**, a dispersion without observable aggregation is indicated for freshly prepared sample. The brightly white droplets nucleated spontaneously from suspension starts to form after 3h (see **Fig S3**). Such droplets that are the so called tactoids were observed in the process of the CNRs liquid crystal assembly also (Wang et al., 2016). Tactoid with short-range ordered structure is considered to act as an intermediate state that bridges the isotropic phase and the liquid crystalline phase (Dumanli et al., 2014; Wang et al., 2016). Figure 4**(b)** shows the details in which the spindle-shaped tactoids of various sizes with 3–4 periodically spaced birefringent lines are distinguished. Tactoids grow and fuse gradually with standing time into the ellipsoidal- or spherical-shaped ones with larger size and increased periodic line as indicated by Fig. 4**(c, d)**. Besides, the intersection between the tactoids during suspension standing is observed as shown in **Fig S4**. With longer standing time, textures with fingerprint-like lines representing the liquid crystals of cellulose are constructed as shown in Fig. 4**(e, f)**. The growth of the tactoids is accompanied by the decrease of the line period from the beginning 3.39 (Fig. 4b) to 1.32 μm (Fig. 4f). Furthermore, time-resolved POM observation combined with the suspension photographs reveals that the internal structure

of the suspension showing turbid (see the inset of Fig. 4) is correlated well with the intermediate tactoid state.

The liquid-crystal organization formed from CNSs suspension was evaluated by POM further. As shown in Fig. 5(a, b), the droplet extracted from the suspension under 6 wt.% concentration loses its iridescent birefringence after covering by the coverslip, the behavior of which is quite different from that of the CNRs (see Fig S5). To the suspension under 12 wt.% concentration as shown in Fig. 5(c, d), a cross-hatch birefringent texture was observed after extrusion. This distinguished pattern was reported recently on the dispersion of CNRs with low aspect ratio (length/width, L/D) and surface charge (Araki et al., 2000; Jiang et al., 2018). It represents the “frozen-in shear structure” in the “birefringent glassy phase” (Araki et al., 1999; Gabriel et al., 1996) arising from the biaxial orientation and the short-range order in the microstructure. Based on previous research combined our observation, it is concluded that the order degree of the liquid-crystal phase assembled from the sphere-like cellulose nanocrystals is not as high as that assembled from the rod-like ones, the reason of which will be discussed in the next section.

It is characteristic that aqueous suspension of the rod-like cellulose nanocrystals can be evaporated to produce solid film in which the liquid crystalline ordering formed in suspension is retained, leading to the iridescent appearance of the film (Lagerwall et al., 2014; Parker et al., 2018; Tao and Xu, 2020). Next it attracts our interest to Fig out the case of sphere-like nanocrystals. The CNSs film was prepared by drying the 6 wt.% suspension in air in 1.5 days. As shown in the **video S1** in the supporting information, the smooth and semi-translucent film as prepared exhibits obvious iridescence in large area. When the film is viewed as close as normal to the film surface against the black background, the bright blue color throughout the whole film is visible (see the inset of Fig. 6a), producing the maximum reflection wavelength (λ_{\max}) of ca. 415 nm in the UV-Vis spectrum as shown in Fig. 6(a). It is noted that the coffee ring effect (Mu and Gray, 2015) which normally induces the changed colors from center to edge of the film evaporated from rod-like CNCs suspension under ambient conditions (see Fig. 8a, d), exerts almost no influence on the CNSs film.

The characteristics of the CNSs assembly in the solid phase was uncovered by POM and SEM. Figure 6(b) shows the POM image of the CNSs film. Polydomains exhibiting unhomogeneous color qualitatively indicate that the liquid-crystalline organization of the CNSs is less order (Shafiei-Sabet et al., 2014). At higher magnification as shown in Fig. 6(c), it is observed the fingerprint texture formed in suspension is retained. The pattern is discontinuous however, which reveals the long-range orientation of the domains is weak. Such discontinuity can be observed more clearly by high-resolution SEM examination as shown by the circles in Fig. 6(d). Moreover, the cross-sectional SEM photograph shows that the CNSs organize in periodically parallel-aligned layer-structure in the solid state which is a typical pattern for the liquid-crystalline self-assembly of CNRs (Parker et al., 2018). The distance (as indicated by the dotted lines) between two neighboring layers is ca. 200 nm.

Distinguished Self-Assembly Characteristics of Sphere-Shaped Cellulose Nanocrystals from Rod-Shaped Ones.

From Chap. 3.1, it is Figd out that the self-assembly of CNSs from suspension to the solid state shows part of similar behavior to CNRs such as the tactoids growth and the layered arrangement, CNSs possess the distinct features as discussed above however. In order to understand the liquid-crystalline assembly of isotropic CNSs, especially the iridescent film normally observed on CNRs, the origin of which is proposed from the parallel alignment of the anisotropic rodlike crystallites (Lagerwall et al., 2014; Parker et al., 2018), the assembly of CNRs having changed aspect ratio will be compared in this chapter.

Table 1
Dimensions, Z potential and crystallinity degree of CNCs in different morphology.

Sample	Average Particle Size (nm)	PDI	Zeta Potential (mV)	CrI ^a (%)
CNSs	78 (d)	0.21	-24	91.0
SCNRs	105 (L)	0.28	-27	85.5
LCNRs	180 (L)	0.42	-30	86.7
a. WAXD profiles of the LCNR and SCNR films are shown in Fig S6b .				

CNRs with sulfate ester groups on the surfaces as proved by FTIR spectra (see **Fig S6a**) were prepared using a comparable preparation strategy of sulfuric acid hydrolysis. Hydrolysis conditions affect the morphology, size, degree of crystallinity (CrI), polydispersity (PDI) and Z potential (which will be discussed in detail later) of the nanocrystals as summarized in Table 1. As shown in Fig. 7(a) and **Fig S6(c)**, the rodlike nanocrystals with 60–160 nm long giving an aspect ratio of 4–18 was named as SCNR. While the nanocrystals with 80–300 nm long giving an aspect ratio of 10–40 was named as SCNR as shown in Fig. 7(b) and **Fig S6(d)**. The self-assembly of the CNRs in suspension is investigated and compared with that of the CNSs subsequently. The aqueous suspension of the sulfate CNRs exhibit typically concentration-dependent lyotropic liquid crystal behavior as shown in Fig. 7(c, d). Above a critical concentration of 5 wt.%, the polydisperse rodlike shape of the cellulose nanocrystals leads to the suspension separation into isotropic and anisotropic phases. As the orientational order of the longer rods is always greater than that of the shorter ones, the longer rods will enrich in the anisotropic phase (Revol et al., 1992). A sharp boundary between the upper isotropic phase and the lower anisotropic one is visible clearly. Phase separation of the SCNRs suspension occurs under 5 wt.% concentration (see Fig. 7c) compared to 5 and 6 wt.% concentration for LCNRs (see Fig. 7d). It proves the biphasic range became narrow to the nanocrystals in reduced aspect ratio (Beck-Candanedo et al., 2005).

More importantly, compared to the organization process of the CNSs liquid crystal as shown in Fig. 3(a), the phase separation is observed particularly on the rodlike cellulose nanocrystals. The viscosity of the CNSs suspension was considered firstly to hinder the phase separation as proposed to the highly viscous suspension of cellulose microcrystals (Gray and Mu, 2015). Shear rheology measurement on the 6 wt.% CNSs suspension was performed accordingly. The steady-state shear viscosity curve is compared with the one collected from the suspension of the rodlike cellulose nanocrystals prepared by sulfuric acid

hydrolysis (Shafiei-Sabet et al., 2014). The dimension of such cellulose nanorods is close to that of our SCNRs. As shown in **Fig S7**, the viscosity profile of our 6 wt.% CNSs suspension exhibit the same changes as the one of the 5 wt.% CNRs suspension reported. Specifically, the viscosity shows three-regional changes as a function of shear rate, including a shear thinning region at low shear rates followed by a plateau at intermediate shear rates, and a second shear thinning at high shear rates. The initial viscosity and its variation range with the shear rate of the CNSs suspension is comparable to that of the reported CNRs suspension which is characterized by the phase separation. Therefore, we consider that both the low polydispersity and the low aspect ratio of the CNSs dimension (see Table 1) other than the high viscosity of the suspension leads to the disappearance of the phase separation which will be discussed further in later.

Organization characteristics of the CNRs in big aspect ratio (LCNRs) and small one (SCNRs) in the solid state is investigated further for the purpose of understanding the liquid-crystalline assembly of CNSs. The films were prepared respectively from the SCNRs and LCNRs suspensions by a comparable preparation strategy to CNSs. Digital photos of the films viewed as close as normal to the film surface against the black background are shown in Fig. 8 (**a, d**). The UV-Vis spectra were collected from the central area of the films which displays the highest ordering (Klockars et al., 2018). The maximum reflection wavelengths of ca. 577 and 698 nm are shown in **Fig S8** for the SCNRs and LCNRs films, respectively in the wavelength range of yellow/green and red light. The color of the films deposited from CNSs (see Fig. 6a), SCNRs, and LCNRs indicates a red-shift as the aspect ratio of the cellulose nanocrystals increases. Moreover, contrast to the CNSs film as shown in Fig. 6(**a**), the coffee ring effect is observed clearly both on the SCNRs and LCNRs films. The impact on the LCNRs film seems greater. In general, suspension drying tends to obtain the films in changed color that red-shift (Mu and Gray, 2015) or blue-shift (Gray and Mu, 2015) radially towards the film edge due to the differential drying rates, the phenomenon of which is responsible for the coffee ring effect. It is concluded accordingly that the flow dynamics in the drying process (Gencer et al., 2017; Mu and Gray, 2015) as well as the self-assembly in the suspension (Uhlig et al., 2016; Wang et al., 2016), both of which are proposed to lead to the final structures in the solid state, are affected by the shape and the dimension of the particles. Further investigation needs to be carried out.

Assembly differences between the CNSs and CNRs in the solid state are revealed by POM and SEM observations. As shown in Fig. 8(**b, e**), color homogeneity of the CNRs films (especially the LCNRs film as shown in Fig. 8e) improves on the micro-scale level compared to the CNSs film (see Fig. 6b), reflecting the better long-range orientation of the CNRs domains. Periodically layer pattern inside the CNRs films observed at higher magnification are shown in Fig. 8(**c, f**). Such layer structure is typical for the liquid-crystal alignment of the rodlike cellulose nanocrystals (Lagerwall et al., 2014). Chiral nematic liquid crystals contain CNC rods arrange in pseudolayers with their long axes parallel to the plane of the layers. The average rod axis direction in each layer, that is the so-called director, is rotated slightly with respect to the neighbouring layers, producing a helical distribution of the pseudolayers. The distance required for the director to make one full rotation about the cholesteric axis is defined as the chiral nematic pitch P which can be evaluated in the cross-sectional SEM photograph. Half the pitch that is the distance

between two dotted lines as shown in Fig. 8(c, f) is estimated to be 282 and 314 nm for SCNRs and LCNRs films, respectively. Combined with the UV-Vis spectra of the films, it proves CNRs in smaller aspect ratio reduce the layer spacing and give film with shorter reflection wavelength. Such trend continues as the aspect ratio decreases further to CNSs (see Fig. 6a, d). Comparing Fig. 8(c, f) to Fig. 6 (d), it is observed that the liquid-crystal organization in CNSs shows distinct pattern from that in CNRs, although the layer structure is identified for all the films. The chiral alignment is weak obviously in CNSs liquid crystals.

The liquid crystalline formation in CNSs suspension was deduced by Cheng et.al before (Wang et al., 2008). It was considered that the combination of the polydispersity and the presence of sulfate groups should play an important role. Herein, based on experimental observation, the difference of the CNSs liquid-crystalline assembly from CNRs, originating from the structural properties of the charged particles, is proposed. Two factors were generally considered to govern the assembly behavior of the cellulose nanocrystals in aqueous suspension: the geometry that is the dimension and aspect ratio of the particles, as well as the surface charge (Beck et al., 2011). As summarized in Table 1, the isotropic CNSs own the smaller particle size, polydispersity (PDI) compared to SCNRs and LCNRs. In another hand, surface charge can be estimated by evaluating the zeta-potential of the suspension (Bertsch et al., 2017). Acid hydrolysis produces nanocrystals with negatively charged groups on the surface, producing a negative zeta-potential. The absolute value of the potential for CNSs suspension is smaller compared to SCNRs and LCNRs, reflecting the decreased number of the surface charge (Parker et al., 2018). It is inevitable for the charge loss in the ultrasonic procedure of CNSs preparation (N. Wang et al., 2008), leading to the fact that the repulsive electrostatic interparticle force resulting from surface charge turns weak whereas the attractive van der Waals forces turns strong accordingly. Considering the CNSs exhibit the similar layered liquid-crystal organization to CNRs as observed above, we propose that the short-range attraction drives CNSs close to each other to form the “knot-like” alignment (see Fig. 9) at the initial stage of the assembly process. The probability of such arrangement is indicated in SEM images as shown in Fig. 10. The “knot-like” pattern is captured in the intermediate state of the CNSs organization in suspension. The negative charges of low loading carried to the CNSs surface originally “delocalized” to the “knot-like” structure surface, leading to a lower surface charge.

Such new structure acts as the fundamental unit for further assembly. With increasing concentration, “knot-like” CNSs aggregate and form tactoids making the suspension turns turbid. The helical charge distribution on surface which governs particle orientation is suggested as the driving force to the liquid-crystal organization of the cellulose nanocrystals (Revol et al., 1992). Within the tactoids, the organization between “knot-like” CNSs units maintain the nematic pattern basically. The decreased excluded volume (the actual excluded volume is considered to be higher than the rod volume due to the charge induced electric double layer (Onsager, 1949)) attributed from less surface charge makes more tightly stacking between “knot-like” units however, leading to a decreased layer period of d_s in CNSs tactoids compared to d_r in CNRs tactoids. It is observed that the layer distance is 2.22 μm for CNSs whereas 4.01 μm for LCNRs (data is not shown). The fusion and precipitation between tactoids proceed

with time. Owing to the excluded volume effect (Buining et al., 1994) also, the suspension including the “knot-like” units in small aspect ratio doesn’t show the phase separation. As the standing time prolongs, the anisotropic liquid-crystal phase was constructed. Gel vitrification occurs upon water evaporation in which the liquid-crystal structures are locked (Dumanli et al., 2014). Such organization can be retained in the film after complete removal of water. Different from CNRs, the weak long-range orientation in CNSs organization is determined by its own structural characteristics. A weaker assembly is observed in the desulfated CNSs film (see **Fig S9**) in which the amount of the CNSs surface charge is reduced further. Moreover, the long and slender particles block each others’ movements to an extent in gel vitrification (Sahimi and Arbabi, 1993). The feature of the geometry uniformity for CNSs may be the reason to showing almost no “coffee-ring” effect in the solid state accordingly.

Conclusions

In the present study, the mechanism of the liquid-crystal assembly for sphere-shaped cellulose nanocrystals (CNSs) was proposed by comparing the organization features of CNSs with that of the rod-shaped nanocrystals (CNRs). Three types of cellulose nanocrystals with high crystallinity were prepared by H_2SO_4 hydrolysis firstly, including the CNSs in an average diameter of ca. 78 nm and the CNRs in changed aspect ratio. The transition from isotropic phase to liquid-crystal phase in CNSs suspension was identified by time-resolved POM combined with the suspension photograph observations. Suspension appearance as a function of time is correlated well with the change of internal phase state. Such phase behavior is similar with the one observed on CNRs but showing the distinguished features. One is that the phase separation occurred in the process of the phase transition which was normally observed in CNRs suspensions disappears. Moreover, the order degree of the liquid-crystal phase assembled from the CNSs is not as high as that assembled from the CNRs.

CNSs assembly in the solid state was discussed further by water evaporation. It is interesting to find that the color of the film as prepared exhibits a blue shift as the aspect ratio decreases from CNRs to CNSs. The morphology observations demonstrate that the liquid-crystal organization characterized by the fingerprint texture formed in suspension is retained. CNSs organize in periodically parallel-aligned layer-structure with a short layer distance of ca. 200 nm in the solid state. High-resolution SEM photograph further indicates a discontinuity showing a weak long-range orientation in each layer. Based on the assembly features of CNSs as well as the isotropic geometry of smaller particle size, lower polydispersity, and lower surface charge than CNRs, we propose a “knot-like” structure at the initial stage of the alignment process, the model of the which is supported by the SEM images. Such new structure acts as the fundamental unit to achieve the liquid-crystal assembly further.

Declarations

ASSOCIATED CONTENT

Supporting Information.

ORCID

Yuan Yuan: 0000-0002-5900-5303, Jianming Zhang: 0000-0003-1602-5010

Author Contributions

[†]Li Cheng and Bingrui Liu contributed equally.

Conflict of interest

The authors declare no competing financial interest.

Acknowledgments

This work was supported by the Natural Science Foundation of China (51903135, 51903134). The authors thank Professor Yan Xu for the in-depth discussion on the assembly mechanism of CNSs.

References

1. Ahmed-Haras MR, Kao N, Ward L (2020) Single-step heterogeneous catalysis production of highly monodisperse spherical nanocrystalline cellulose. *Int J Biol Macromol* 154:246–255. <https://doi.org/10.1016/j.ijbiomac.2020.02.298>
2. Al Hakkak J, Grigsby WJ, Kathirgamanathan K, Edmonds NR (2019) Generation of Spherical Cellulose Nanoparticles from Ionic Liquid Processing via Novel Nonsolvent Addition and Drying. *Advances in Materials Science and Engineering*, 2019, 1–6. <https://doi.org/10.1155/2019/2081027>
3. Araki J, Wada M, Kuga S, Okano T (1999) Influence of surface charge on viscosity behavior of cellulose microcrystal suspension. *Journal of Wood Science* 45(3):258–261. <https://doi.org/10.1007/BF01177736>
4. Araki J, Wada M, Kuga S, Okano T (2000) Birefringent glassy phase of a cellulose microcrystal suspension. *Langmuir* 16(6):2413–2415. <https://doi.org/10.1021/la9911180>
5. Azrina ZZ, Beg MDH, Rosli M, Ramli R, Junadi N, Alam AM (2017) Spherical nanocrystalline cellulose (NCC) from oil palm empty fruit bunch pulp via ultrasound assisted hydrolysis. *Carbohydr Polym* 162:115–120. <http://dx.doi.org/10.1016/j.carbpol.2017.01.035>
6. Azubuike CP, Rodríguez H, Okhamafe AO, Rogers RD (2011) Physicochemical properties of maize cob cellulose powders reconstituted from ionic liquid solution. *Cellulose* 19(2):425–433. <https://doi.org/10.1007/s10570-011-9631-y>
7. Babicka M, Wozniak M, Dwiecki K, Borysiak S, Ratajczak I (2020) Preparation of Nanocellulose Using Ionic Liquids: 1-Propyl-3-Methylimidazolium Chloride and 1-Ethyl-3-Methylimidazolium Chloride. *Molecules* 25(7). <https://doi.org/10.3390/molecules25071544>
8. Beck-Candanedo S, Roman M, Gray DG (2005) Effect of reaction conditions on the properties and behavior of wood cellulose nanocrystal suspensions. *Biomacromolecules* 6(2):1048–1054.

<https://doi.org/10.1021/bm049300p>

9. Beck S, Bouchard J, Berry R (2011) Controlling the reflection wavelength of iridescent solid films of nanocrystalline cellulose. *Biomacromolecules* 12(1):167–172. <https://doi.org/10.1021/bm1010905>
10. Bertsch P, Isabetini S, Fischer P (2017) Ion-Induced Hydrogel Formation and Nematic Ordering of Nanocrystalline Cellulose Suspensions. *Biomacromolecules* 18(12):4060–4066
11. Buining P, Philipse A, Lekkerkerker H (1994) Phase behavior of aqueous dispersions of colloidal boehmite rods. *Langmuir* 10(7):2106–2114. <https://doi.org/10.1021/acs.biomac.7b01119>
12. Cheng M, Qin ZY, Liu YN, Qin YF, Li T, Chen L, Zhu MF (2014) Efficient extraction of carboxylated spherical cellulose nanocrystals with narrow distribution through hydrolysis of lyocell fibers by using ammonium persulfate as an oxidant. *J Mater Chem A* 2(1):251–258. <https://doi.org/10.1039/c3ta13653a>
13. Dumanli AG, Kamita G, Landman J, van der Kooij H, Glover BJ, Baumberg JJ, Steiner U, Vignolini S (2014) Controlled, Bio-inspired Self-Assembly of Cellulose-Based Chiral Reflectors. *Adv Opt Mater* 2(7):646–650. <https://doi.org/10.1002/adom.201400112>
14. Filson PB, Dawson-Andoh BE (2009) Sono-chemical preparation of cellulose nanocrystals from lignocellulose derived materials. *Bioresour Technol* 100(7):2259–2264. <https://doi.org/10.1016/j.biortech.2008.09.062>
15. Gabriel J-CP, Sanchez C, Davidson P (1996) Observation of nematic liquid-crystal textures in aqueous gels of smectite clays. *J Phys Chem* 100(26):11139–11143. <https://doi.org/10.1021/jp961088z>
16. Gencer A, Schutz C, Thielemans W (2017) Influence of the Particle Concentration and Marangoni Flow on the Formation of Cellulose Nanocrystal Films. *Langmuir* 33(1):228–234. <https://doi.org/10.1021/acs.langmuir.6b03724>
17. Gray DG, Mu X (2015) *Mater (Basel)* 8(11):7873–7888. <https://doi.org/10.3390/ma8115427>. Chiral Nematic Structure of Cellulose Nanocrystal Suspensions and Films; Polarized Light and Atomic Force Microscopy
18. Han J, Zhou C, French AD, Han G, Wu Q (2013) Characterization of cellulose II nanoparticles regenerated from 1-butyl-3-methylimidazolium chloride. *Carbohydr Polym* 94(2):773–781. <https://doi.org/10.1016/j.carbpol.2013.02.003>
19. Hasegawa H, Horikawa Y, Shikata T (2020) Cellulose Nanocrystals as a Model Substance for Rigid Rod Particle Suspension Rheology. *Macromolecules* 53(7):2677–2685. <https://doi.org/10.1021/acs.macromol.9b02641>
20. Jiang M, McMillan MF, Davis V, Kitchens CL (2018) Phase Behavior of Acetylated Cellulose Nanocrystals and Origins of the Cross-Hatch Birefringent Texture. *Biomacromolecules* 19(8):3435–3444. <https://doi.org/10.1021/acs.biomac.8b00746>
21. Klemm D, Kramer F, Moritz S, Lindstrom T, Ankerfors M, Gray D, Dorris A (2011) Nanocelluloses: a new family of nature-based materials. *Angew Chem Int Ed* 50(24):5438–5466. <https://doi.org/10.1002/anie.201001273>

22. Klockars KW, Tardy BL, Borghei M, Tripathi A, Greca LG, Rojas OJ (2018) Effect of Anisotropy of Cellulose Nanocrystal Suspensions on Stratification, Domain Structure Formation, and Structural Colors. *Biomacromolecules* 19(7):2931–2943. <https://doi.org/10.1021/acs.biomac.8b00497>
23. Lagerwall JPF, Schutz C, Salajkova M, Noh J, Park JH, Scalia G, Bergstrom L (2014) Cellulose nanocrystal-based materials: from liquid crystal self-assembly and glass formation to multifunctional thin films. *NPG Asia Materials* 6(1):e80–e80. <https://doi.org/10.1038/am.2013.69>
24. Li XF, Ding E-y, Li GK (2001) A method of preparing spherical nano-crystal cellulose with mixed crystalline forms of cellulose I and II. *Chin J Polym Sci* 19(3):291–296
25. Liu Y, Liu L, Wang K, Zhang H, Yuan Y, Wei H, Wang X, Duan Y, Zhou L, Zhang J (2020) Modified ammonium persulfate oxidations for efficient preparation of carboxylated cellulose nanocrystals. *Carbohydr Polym* 229:115572. <https://doi.org/10.1016/j.carbpol.2019.115572>
26. Lu P, Hsieh YL (2010) Preparation and properties of cellulose nanocrystals: Rods, spheres, and network. *Carbohydr Polym* 82(2):329–336. <https://doi.org/10.1016/j.carbpol.2010.04.073>
27. Mahmud MM, Perveen A, Jahan RA, Matin MA, Wong SY, Li X, Arafat MT (2019) Preparation of different polymorphs of cellulose from different acid hydrolysis medium. *Int J Biol Macromol* 130:969–976. <https://doi.org/10.1016/j.ijbiomac.2019.03.027>
28. Meyabadi TF, Dadashian F, Sadeghi GMM, Asl HEZ (2014) Spherical cellulose nanoparticles preparation from waste cotton using a green method. *Powder Technol* 261:232–240. <http://dx.doi.org/10.1016/j.powtec.2014.04.039>
29. Mu XY, Gray DG (2015) Droplets of cellulose nanocrystal suspensions on drying give iridescent 3-D "coffee-stain" rings. *Cellulose* 22(2):1103–1107. <https://doi.org/10.1007/s10570-015-0569-3>
30. Mukherjee SM, Woods HJ (1953) X-ray and electron microscope studies of the degradation of cellulose by sulphuric acid. *Biochim Biophys Acta* 10(4):499–511. [https://doi.org/10.1016/0006-3002\(53\)90295-9](https://doi.org/10.1016/0006-3002(53)90295-9)
31. Onsager L (1949) The Effects of Shape on the Interaction of Colloidal Particles. *Ann N Y Acad Sci* 51(4):627–659. <https://doi.org/10.1111/j.1749-6632.1949.tb27296.x>
32. Parker RM, Guidetti G, Williams CA, Zhao T, Narkevicius A, Vignolini S, Frka-Petesic B (2018) The Self-Assembly of Cellulose Nanocrystals: Hierarchical Design of Visual Appearance. *Adv Mater* 30(19):e1704477. <https://doi.org/10.1002/adma.201704477>
33. Prathapan R, Tabor RF, Garnier G, Hu J (2020) Recent progress in cellulose nanocrystal alignment and its applications. *ACS Appl Bio Mater* 3(4):1828–1844. <https://doi.org/10.1021/acsabm.0c00104>
34. Revol JF, Bradford H, Giasson J, Marchessault RH, Gray DG (1992) Helicoidal self-ordering of cellulose microfibrils in aqueous suspension. *Int J Biol Macromol* 14(3):170–172. [https://doi.org/10.1016/s0141-8130\(05\)80008-x](https://doi.org/10.1016/s0141-8130(05)80008-x)
35. Sahimi M, Arbabi S (1993) Mechanics of disordered solids. II. Percolation on elastic networks with bond-bending forces. *Phys Rev B* 47(2):703–712. <https://doi.org/10.1103/physrevb.47.703>
36. Satyamurthy P, Vigneshwaran N (2013) A novel process for synthesis of spherical nanocellulose by controlled hydrolysis of microcrystalline cellulose using anaerobic microbial consortium. *Enzym*

- Microb Technol 52(1):20–25. <https://doi.org/10.1016/j.enzmictec.2012.09.002>
37. Segal L, Creely JJ, Jr M, Conrad C (1959) An empirical method for estimating the degree of crystallinity of native cellulose using the X-ray diffractometer. *Text Res J* 29(10):786–794. <https://doi.org/10.1177/004051755902901003>
38. Shafiei-Sabet S, Hamad WY, Hatzikiriakos SG (2014) Ionic strength effects on the microstructure and shear rheology of cellulose nanocrystal suspensions. *Cellulose* 21(5):3347–3359. <https://doi.org/10.1007/s10570-014-0407-z>
39. Sui XF, Yuan JY, Yuan WZ, Zhou M (2008) Preparation of cellulose nanofibers/nanoparticles via electrospray. *Chem Lett* 37(1):114–115. <https://doi.org/10.1246/cl.2008.114>
40. Tao J, Xu Y (2020) Cellulose Nanocrystals-based Chiroptical Materials. *Paper and Biomaterial* 5:14–30. <https://doi.org/10.12103/j.issn.2096-2355.2020.03.002>
41. Uhlig M, Fall A, Wellert S, Lehmann M, Prevost S, Wagberg L, von Klitzing R, Nystrom G (2016) Two-Dimensional Aggregation and Semidilute Ordering in Cellulose Nanocrystals. *Langmuir* 32(2):442–450. <https://doi.org/10.1021/acs.langmuir.5b04008>
42. Ureña-Benavides EE, Ao G, Davis VA, Kitchens CL (2011) Rheology and Phase Behavior of Lyotropic Cellulose Nanocrystal Suspensions. *Macromolecules* 44(22):8990–8998. <https://doi.org/10.1021/ma201649f>
43. Wang N, Ding E, Cheng R (2007) Thermal degradation behaviors of spherical cellulose nanocrystals with sulfate groups. *Polymer* 48(12):3486–3493. <https://doi.org/10.1016/j.polymer.2007.03.062>
44. Wang N, Ding E, Cheng R (2008) Preparation and liquid crystalline properties of spherical cellulose nanocrystals. *Langmuir* 24(1):5–8. <https://doi.org/10.1021/la702923w>
45. Wang PX, Hamad WY, MacLachlan MJ (2016) Structure and transformation of tactoids in cellulose nanocrystal suspensions. *Nat Commun* 7:11515. <https://doi.org/10.1038/ncomms11515>
46. Wang Z, Yuan Y, Hu J, Yang J, Feng F, Yu Y, Men Y, Zhang J (2020) Origin of vacuum-assisted chiral self-assembly of cellulose nanocrystals. *Carbohydr Polym* 245:116459. <https://doi.org/10.1016/j.carbpol.2020.116459>
47. Xie HX, Du HS, Yang XG, Si CL (2018) Recent Strategies in Preparation of Cellulose Nanocrystals and Cellulose Nanofibrils Derived from Raw Cellulose Materials. *International Journal of Polymer Science*, 2018, 1–25. <https://doi.org/10.1155/2018/7923068>
48. Yu HY, Yan CF, Lei XX, Qin ZY, Yao JM (2014) Novel approach to extract thermally stable cellulose nanospheres with high yield. *Mater Lett* 131:12–15. <https://doi.org/10.1016/j.matlet.2014.05.159>
49. Zero K, Pecora R (1982) Rotational and translational diffusion in semidilute solutions of rigid-rod macromolecules. *Macromolecules* 15(1):87–93. <https://doi.org/10.1021/ma00229a017>
50. Zhang J, Elder TJ, Pu Y, Ragauskas AJ (2007) Facile synthesis of spherical cellulose nanoparticles. *Carbohydr Polym* 69(3):607–611. <https://doi.org/10.1016/j.carbpol.2007.01.019>
51. Zhou LJ, Li N, Shu J, Liu YX, Wang KT, Cui X, Yuan Y, Ding B, Geng Y, Wang Z, Duan Y, Zhang JM (2018) One-Pot Preparation of Carboxylated Cellulose Nanocrystals and Their Liquid Crystalline

Behaviors. ACS Sustain Chem Eng 6(9):12403–12410.

<https://doi.org/10.1021/acssuschemeng.8b02926>

52. Zianor Azrina ZA, Beg MDH, Rosli MY, Ramli R, Junadi N, Alam A (2017) Spherical nanocrystalline cellulose (NCC) from oil palm empty fruit bunch pulp via ultrasound assisted hydrolysis. Carbohydr Polym 162:115–120. <https://doi.org/10.1016/j.carbpol.2017.01.035>

Figures



Figure 1

Schematic of the CNSs preparation process.

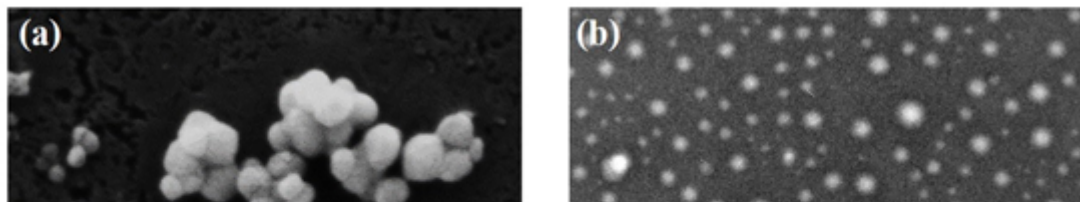


Figure 2

(a, b) SEM (a) and TEM (b) images of the CNSs. (c) The statistical distribution of the CNSs diameters from the TEM image. (d) WAXD profile of the CNSs powder.

Figure 3

(a) Images of CNSs suspensions from 0.5 to 6 wt.% concentration photographed between cross-polarizers after equilibration for 15 days. The cuvette is 5 mm in thickness. (b) CNSs apparent translation diffusion coefficient (\square) and hydrodynamic diameter (Δ) as a function of suspension concentration measured by DLS. Error bars represent the standard deviations of three replicate measurements.



Figure 4

Time resolved POM images of 5 wt.% CNSs suspension. Scale bars are 50 μm . Insets are corresponding images of CNSs suspension photographed between cross-polarizers. The cuvette is 5 mm in thickness.



Figure 5

POM images of CNSs droplets photographed to the 6 (a, b) and 12 wt.% (c, d) samples without (a, c) and with coverslip covering (b, d).

Figure 6

(a) UV-Vis transmission spectrum of the CNSs film. Inset is the photograph of the CNSs film evaporated from 6 wt.% suspension under ambient conditions. The image is photographed at a normal angle to the film surface. (b, c) POM image of the CNSs film photographed at different magnification. (d) The cross-sectional SEM image of the CNSs film. The circles in dotted lines marks the discontinuous part of the layer structure.

Figure 7

(a) AFM images of the rod-like cellulose nanocrystals in small aspect ratio SCNR (a) and large aspect ratio LCNR (b). (c, d) Images of SCNR (c) and LCNR (d) suspensions from 4, 5, 6 and 7 wt.% concentration (from left to right) photographed between cross-polarizers after equilibration for 5 days. The cuvette is 5 mm in thickness.



Figure 8

(a, d) The photograph of the SCNRs (a) and LCNRs (d) films evaporated from 6 wt.% suspensions under ambient conditions. The images are photographed at a normal angle to the film surface. (b, e) POM images of the SCNRs (b) and LCNRs (e) films. (c, f) The cross-sectional SEM images of the SCNRs (c) and LCNRs (f) films.



Figure 9

Schematic representation of the liquid-crystal self-assembly process of CNSs and CNRs. d_s and denotes the layer period of the CNSs assembly in the liquid state and in the solid state, respectively. d_R and d'_R denotes the corresponding period for CNRs.



Figure 10

The SEM images of the CNC–PAAm composite hydrogels showing the intermediate state of the CNSs assembly. The structures of CNSs assembly in 12h (a, b) and 3 days (c) are shown. The “knot-like” structure is denoted by the yellow circles in dotted lines.

Supplementary Files

This is a list of supplementary files associated with this preprint. Click to download.

- [FigureS8bcopyright.pdf](#)
- [GraphicalAbstract.docx](#)
- [Hightlights.doc](#)
- [VideoS1.mp4](#)
- [supportinginformation.docx](#)